Research Article

Shengzhao Wang*, Jinfan Song and Bin Liu

Investigation of thermal conductivity and Raman spectra for HfAlB, TaAlB, and WAlB based on first-principles calculations

Abstract: The Raman spectra, thermal conductivity, and related physical properties of three MAB materials HfAlB, TaAlB, and WAlB are investigated by using first-principles calculations. The results reveal that all three materials possess a metallic layered structure, characterized by alternating stacks of network layers composed of transition metals M, B, and Al layers. The strong covalent bonds between B atoms and the metallic bonds of M−Al collectively determine the stability and electrical conductivity of these materials. In terms of lattice thermal conductivity, TaAlB (34.0 W/(m K)) and HfAlB (16.9 W/(m K)) exhibit relatively high values, while WAlB (3.5 W/(m K)) shows significantly smaller thermal conductivity due to enhanced phonon scattering resulting from strong anharmonicity. Raman spectroscopic analysis reveals the presence of nine Raman-active modes in each material. The peaks at low frequencies correspond to the vibrational modes of M and Al atoms, whereas the peaks at high frequencies are associated with the stretching vibrations of covalent bonds within B atoms. Furthermore, HfAlB and TaAlB demonstrate reduced phonon scattering, which aligns with their thermal conductivity results. Notably, this study elucidates the intrinsic relationships among atomic structures, chemical bonds, and thermal transport properties, thereby providing a theoretical foundation for the use of MAB materials in high-temperature applications, including thermal conduction and thermal barrier coatings.

1 Introduction

MAB materials, where M represents a transition metal, A stands for aluminum, and B denotes boron, are emerging as a class of layered ternary borides. Due to their unique crystal structures and potentially exceptional properties, such as high melting points and excellent electrical conductivity [1–3], they have garnered significant research interest. MAB materials exhibit characteristics of both metals and ceramics, including high melting points, favorable thermal and electrical conductivity, and remarkable high-temperature resistance [4–6]. These properties provide them with extensive application prospects in high-temperature fields, such as coatings for thermal barrier applications, high-temperature structural materials, and nuclear reactor components [7].

Investigating the Raman spectra and thermal conductivity of MAB materials is of significant scientific importance and holds considerable potential for applications, particularly in the field of high-temperature materials. Raman spectra is an effective tool for studying the vibrational modes of materials. By simulating Raman spectra both experimentally and theoretically (through first-principles calculations), researchers can gain in-depth insights into the phonon vibrational modes of materials, thereby revealing the relationships between their microscopic structures and vibrational characteristics [8]. This information is essential for understanding the thermal properties of materials.

The first-principles approach allows for an accurate description of the electronic structures and vibrational properties of materials at the quantum mechanical level.

---

*Corresponding author: Shengzhao Wang, Nanyang Institute of Technology, School of Mathematics and Physics, No. 80 Changjiang Road, Nanyang, 473004, Henan, China; and Henan Province Engineering Technology Research Center of New Optoelectronic and Storage Materials, No. 80 Changjiang Road, Nanyang, 473004, Henan, China,
E-mail: shengzw@nyist.edu.cn. https://orcid.org/0000-0003-0779-730X
Jinfan Song, Nanyang Institute of Technology, School of Mathematics and Physics, No. 80 Changjiang Road, Nanyang, 473004, Henan, China; and Henan Province Engineering Technology Research Center of New Optoelectronic and Storage Materials, No. 80 Changjiang Road, Nanyang, 473004, Henan, China
Bin Liu, Nanyang Institute of Technology, School of Mathematics and Physics, No. 80 Changjiang Road, Nanyang, 473004, Henan, China

This method provides a solid theoretical foundation for exploring the physical properties of materials [9]. First-principles calculations can predict the thermal conductivity of MAB materials and analyze key factors that influence thermal conductivity, such as phonon scattering and lattice structures [10–15]. By guiding experimental research with theoretical predictions, the thermal conductivity of materials can be optimized to meet specific application requirements. Additionally, by integrating first-principles studies of Raman spectra and thermal conductivity, a comprehensive understanding of the relationships among the structural, vibrational, and thermal transport properties of MAB materials can be attained. This approach offers theoretical guidance for exploring novel high-temperature materials, directing experimental research, and facilitating material design, ultimately advancing both material design and applications [16–18].

The unique properties of MAB phase materials, including their high-temperature mechanical performance, resistance to high-temperature oxidation, low-temperature synthesis capability, and machinability, provide significant application potential across multiple fields [19–21]. Research has shown that MAB phase materials, such as WAlB, exhibit metallic characteristics. By analyzing the electronic band structure and density of states (DOS), one can gain comprehensive insights into the electronic behavior of these materials. Methods such as the electron localization function (ELF) and Bader's quantum theory of atoms in molecules have the potential to elucidate the nature of B–B covalent bonds, as well as the intermediate covalent-metallic bonding between M and B [22]. Thermal conductivity is a critical physical property of MAB phase materials, especially in high-temperature applications [23–25]. When combined with the Boltzmann transport equation (BTE), first-principles calculations can accurately predict the thermal conductivity of materials and offer insights for optimizing their thermal performance [26–29]. Furthermore, first-principles calculations can predict Raman spectra and assist in interpreting experimental results [30–32].

Although some studies have been conducted on MAB phases, first-principles investigations into the Raman spectra and thermal conductivity of representative MAB materials – namely HfAlB, TaAlB, and WAlB – remain relatively scarce. Therefore, employing first-principles methods to study the Raman spectra and thermal conductivity of MAlB (M = Hf, Ta, and W) serves a dual purpose. On one hand, it allows for precise predictions of the lattice vibrational modes and thermal conductivity of these materials, thereby bridging gaps in experimental research. On the other hand, it enables a comprehensive analysis of the intrinsic relationships among atomic structures, chemical bonding characteristics, Raman spectra, and thermal conductivity, thereby providing theoretical support for interpreting experimental phenomena. Furthermore, theoretical calculations can guide the design and performance optimization of novel boride materials, assisting in overcoming performance bottlenecks in existing materials for practical applications. This, in turn, fosters technological innovations in fields such as high-temperature structural materials and electronic heat dissipation materials.

2 Methodology

In this study, first-principles calculations based on density functional theory (DFT) were executed via the VASP software package for simulations. The exchange-correlation energy was addressed with the Perdew-Burke-Ernzerhof (PBE) functional in conjunction with the generalized gradient approximation (GGA). The plane-wave cutoff energy was set to 700 eV. For both geometric optimization and electronic property calculations, a $13 \times 13 \times 13$ Monkhorst-Pack k-point sampling scheme was employed. To ensure computational accuracy, the energy convergence criterion for structural optimization was established at 1×10^{-8} eV, while the atomic force convergence criterion was set to 1×10^{-7} eV/Å [33–35]. And the valence electron configurations for each element in the calculation are as follows: Hf has a configuration of $5d^2 6s^2$, Ta has $5d^3 6s^2$, W has $5d^4 6s^2$, Al has $3s^2 3p^1$, and B has $2s^2 2p^1$.

The thermal properties and phonon-related characteristics were calculated using VASP in conjunction with software ShengBTE [36, 37]. During the calculation process, Phonopy and Thirdorder software played crucial roles [38]. By employing VASP alongside Phonopy, Density Functional Perturbation Theory (DFPT) was utilized to perform $4 \times 4 \times 4$ supercell calculations with $17 \times 17 \times 17$ Monkhorst-Pack k-point and $20 \times 20 \times 20$ q-mesh (MP) for HfAlB, TaAlB, and WAlB. The second-order force constant matrices was obtained. The force constant matrix is constructed using Phonopy. The symmetry reduction function is enabled to minimize redundant calculations, while built-in symmetry constraints ensure that the force constant matrix satisfies translational invariance. At the same time, the LESPILON = TRUE keyword is used in the article to account for LO-TO splitting and to calculate Raman and infrared spectra. And the Thirdorder program was utilized to perform $3 \times 3 \times 3$ supercell calculations with $13 \times 13 \times 13$ Monkhorst-Pack k-point for these materials, considering at least 13 neighboring atoms to ensure
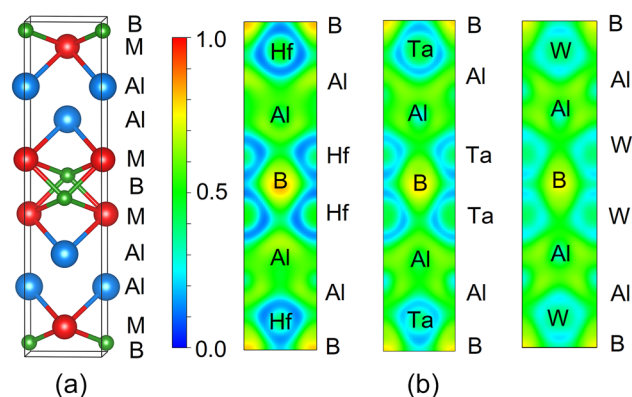
Figure 1: Structure diagram (a), and ELF (b) of HfAlB, TaAlB and WAlB.

convergence. Subsequently, by integrating the second-order and third-order force constant matrices, the ShengBTE program was employed to evaluate the thermal transport properties of HfAlB, TaAlB, and WAlB. For the calculation of Raman and IR spectroscopic properties, a methodology that combined Phonopy, Phono3py, and Phonopy-spectroscopy software was adopted [39].

3 Results and discussion

3.1 Crystal structure

As illustrated in Figure 1(a), the schematic diagrams of the unit cells for HfAlB, TaAlB, and WAlB are presented. These diagrams show a two-dimensional network of layers composed of metal M (depicted in red) and boron (shown in green) atoms, which alternate with aluminum (represented in blue) layers.

The lattice parameters of MAlB are detailed in Table 1, with $\alpha = \beta = \gamma = 90°$. For HfAlB, TaAlB, and WAlB, the values of parameters a and b exhibit a successive decrease as the M element transitions from Hf to Ta and then to W. This trend is closely related to the reduction in the atomic radius of the M element. The decrease in parameters a and b results in a closer packing of atoms along these directions, which in turn affects the chemical bonds and other related properties. This modification has the potential to cause changes in both the atomic arrangement density and the interlayer

Table 1: Calculated lattice parameters of MAlB materials.

MAlB materials	a(Å)	b(Å)	c(Å)
HfAlB	3.455	15.539	3.153
TaAlB	3.341	14.643	3.100
WAlB	3.220	13.999	3.123

interactions. Additionally, parameter c decreases in the order of HfAlB, WAlB, and TaAlB. HfAlB, TaAlB, and WAlB exhibit a nanolayered ternary boride structure characterized by a space group of *Cmcm* (No. 63).

The crystal structures HfAlB, TaAlB, and WAlB display distinctive features. From the perspective of crystal structural characteristics, the fundamental structural unit of the MAlB phase consists of network layers formed by transition metal M and B atoms, alternating with stacked Al atomic layers. This layered architecture is the underlying reason for the unique properties exhibited by MAlB compounds.

The transition metal M atoms are arranged in a prismatic configuration, with chains of B atoms positioned at the centers of these prisms, creating a distinctive prismatic coordination environment. This environment significantly influences the interactions between M and B, thereby impacting the overall properties of the material. In the MAlB structure, boron atoms form chain-like structures, where they are tightly bonded to one another through covalent bonds. This strong interaction provides a solid foundation for the structural stability and hardness of the material. Additionally, the two layers of Al atoms intercalated between the M−B layers play a crucial role. The aluminum layers not only facilitate close atomic bonding through metallic interactions but also contribute electrons, significantly affecting the material's electrical conductivity and other physical properties.

In terms of bonding characteristics, the bonding nature of HfAlB, TaAlB, and WAlB is relatively complex, resulting from a hybrid interaction of covalent, metallic, and ionic bonds. The covalent bonds between the metal and boron atoms within the M−B layers, as well as those among the boron atoms themselves, constitute the primary bonding interactions in the MAlB structure, endowing the material with high hardness and exceptional stability. The aluminum atoms within the aluminum layers are bonded through metallic bonds, which not only provide the material with excellent electrical conductivity but also, in conjunction with transition metal atoms, further enhance the overall strength and toughness of the material. Additionally, there is a degree of charge transfer between the M−B layers and the Al layers, resulting in ionic bonding. This ionic interaction contributes to the structural stability and influences the electronic properties of the material. As illustrated in Figure 1(b), the bonding characteristics on the MAlB (001) surface can be analyzed using the ELF. In the ELF distribution graph, different values represent specific electron behaviors. A value of 1 indicates that electrons are fully localized in one region. A value of 0.5 signifies that electrons are evenly delocalized, while a value of 0 means there
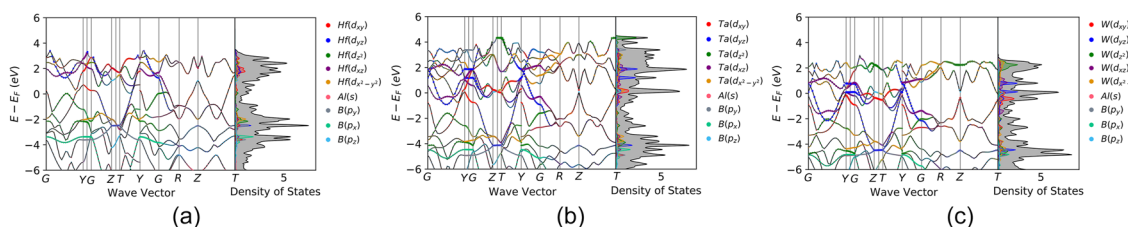
Figure 2: Electronic band of HfAlB (a), TaAlB (b), WAlB (c).

are virtually no electrons present in that area [40]. Studies have found that in this structure, all the ions – M, Al, and B – are surrounded by a uniformly distributed electron "cloud," represented by the green area in the graph. The B atoms are connected by covalent bonds, which are strong chemical bonds. The bond between M and B is also covalent but relatively weaker. Between M and Al, there exists a special type of electron "gas" exhibiting properties similar to those of a metallic bond. The presence of an M atom may disrupt the interaction between Al and B, thereby promoting the formation of localized electrons. However, due to this unique nano-layered ternary boride structure, Al can be easily exfoliated or etched to form MBene materials.

3.2 Electronic band properties

As shown in Figure 2, the electronic band diagrams of HfAlB, TaAlB, and WAlB show no bandgap near the Fermi level, with multiple overlaps between the valence band and the conduction band, confirming their metallic nature. The projected density of states (PDOS) analysis for HfAlB, TaAlB, and WAlB indicates that the density of states (DOS) near the Fermi level is primarily contributed by the d-orbital electrons of Hf, Ta, and W, with a minor contribution from the p-orbitals of B, while the contribution from Al is negligible. This suggests that the first three elements significantly influence the electrical conductivity of MAlB materials. Within the energy range of the valence band near the Fermi level, the hybridization between the p-orbital of B and the d-orbitals of hafnium (Hf), tantalum (Ta), and tungsten (W) is stronger than that between the p-orbital of Al and

the d-orbitals of Hf, Ta, and W. This suggests that there is a stronger covalent bonding between Hf, Ta, W, and B. Such differences in bonding may influence the elastic modulus of the materials, as stronger covalent bonds typically enhance hardness and stiffness. Although HfAlB, TaAlB, and WAlB share similar crystal structures, subtle differences exist in their energy band structures and density of states (DOS) due to the unique electronic configurations of the transition metals Hf, Ta, and W. These differences may subsequently affect their electrical conductivity, thermal stability, and mechanical properties.

3.3 Crystal stability

3.3.1 Phonon dispersion

As shown in Figure 3, the phonon dispersion of HfAlB, TaAlB, and WAlB show no imaginary frequencies, indicating their dynamical stability. The primitive cells of these compounds consist of 2 metal (Hf, Ta, or W) atoms, 2 Al atoms, and 2 B atoms. Their phonon dispersion include 3 acoustic branches and 15 optical branches. The acoustic branches exhibit approximately linear behavior near the Γ point, which is consistent with the characteristics of typical acoustic modes. In HfAlB, TaAlB, and WAlB, the lower vibrations are primarily attributed to the M and Al atoms, while the high-frequency region is predominantly influenced by the lighter B atoms. This indicates that B atoms, due to their small mass and strong covalent bonds, tend to vibrate at higher frequencies, whereas the heavier M and Al atoms dominate the low-frequency acoustic branches. The relatively low mass and strong bonding of B atoms result
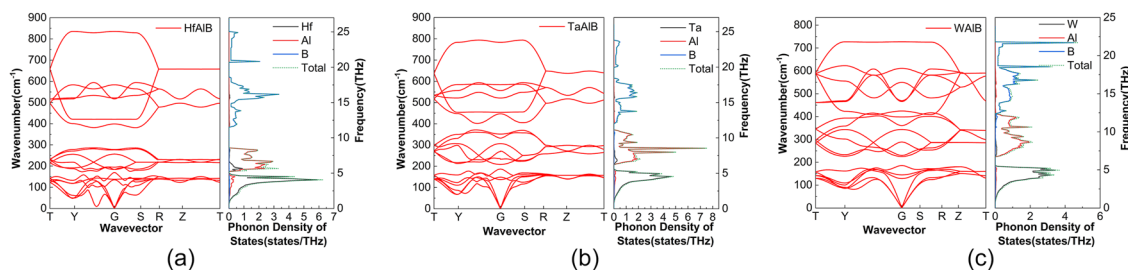

Figure 3: Phonon dispersion of HfAlB (a), TaAlB (b), WAlB (c).

Table 2: Calculated material elastic constants.

Materials	C_{11}	C_{12}	C_{13}	C_{22}	C_{23}	C_{33}	C_{44}	C_{55}	C_{66}
HfAlB	248.71	103.29	83.78	177.05	79.94	326.80	102.61	136.95	92.59
TaAlB	293.68	139.02	159.07	272.57	117.28	359.59	162.62	181.11	179.39
WAlB	356.27	156.25	175.33	351.71	146.09	397.70	194.70	169.41	180.79

in high vibrational frequencies, while the heavier Hf, Ta, and W atoms exhibit lower vibrational frequencies. This characteristic presents significant potential for tuning the phonon bandgap by adjusting the types or ratios of atoms, thereby influencing the material's thermal properties, such as thermal conductivity and the coefficient of thermal expansion.

3.3.2 Mechanical stability

$$C_{11} > 0, C_{11}C_{22} > C_{12}^2,$$
$$C_{44} > 0, C_{55} > 0, C_{66} > 0,$$
$$C_{11}C_{22}C_{33} + 2C_{12}C_{13}C_{23}$$
$$-C_{11}C_{23}^2 - C_{22}C_{13}^2 - C_{33}C_{12}^2 > 0 \qquad (1)$$

The mechanical stability assessment of HfAlB, TaAlB, and WAlB materials with the *Cmcm* (No. 63) structure is presented in Table 2. In the *Cmcm* crystal system, nine independent elastic constants – C_{11}, C_{12}, C_{13}, C_{22}, C_{23}, C_{33}, C_{44}, C_{55}, and C_{66} – are critical. Ensuring that a material satisfies the conditions outlined in Equation (1) is a fundamental step in confirming its mechanical stability, which is essential for the practical application and further development of these materials. The detailed calculation results of the elastic constants for these three materials, presented in Table 2, indicate that HfAlB, TaAlB, and WAlB all satisfy the prerequisites for achieving mechanical stability, confirming their mechanical stability.

3.4 Lattice thermal conductivity

In fact, the temperature gradient ∇T can produce a non-zero heat flux J. In the linear range, the thermal conductivity κ is defined by the equation $J^\alpha = -\sum_\beta \kappa^{\alpha\beta}(\nabla T)^\beta$. The heat flow J can be expressed as follows:

$$J = \sum_p \int f_\lambda \hbar \omega_\lambda v_\lambda \frac{\mathrm{d}\boldsymbol{q}}{(2\pi)^3} \qquad (2)$$

where p is the category identifier of the phonon branch. q is the wave vector. The variable ω_λ employed to denote the angular frequency of phonon mode λ, $\boldsymbol{v}_\lambda$ denotes the group velocity of phonon mode λ, and f_λ is the phonon

distribution function. In the case of thermal equilibrium with no temperature gradient, phonons are distributed according to Bose–Einstein statistics $f_0(\omega_\lambda)$. However, when a temperature gradient ∇T is present, the phonon distribution deviates from the Bose–Einstein statistical distribution. This deviation can be described using the BTE. In the steady state, the rate of change of the distribution must approach zero, as expressed by the BTE.

$$\frac{\mathrm{d}f_\lambda}{\mathrm{d}t} = \frac{\partial f_\lambda}{\partial t}\bigg|_{\text{diffusion}} + \frac{\partial f_\lambda}{\partial t}\bigg|_{\text{scattering}} = 0 \qquad (3)$$

Here $\frac{\partial f_\lambda}{\partial t}\big|_{\text{diffusion}} = -\nabla T \cdot \boldsymbol{v}_\lambda \frac{\partial f_\lambda}{\partial T}$, and $\frac{\partial f_\lambda}{\partial t}\big|_{\text{scattering}}$ is determined by the specific scattering process, which can be analyzed in the framework of perturbation theory. In most practical cases, the range of ∇T is small enough so that f_λ can be expanded to the first order in ∇T, so that $f_\lambda = f_0(\omega_\lambda) + g_\lambda$, where g_λ is linearly related to ∇T. This dependence can be expressed as $g_\lambda = -F_\lambda \cdot \nabla T \frac{\mathrm{d}f_0}{\mathrm{d}T}$. When the only scattering sources are two-phonon and three-phonon processes, the resulting linear BTE can be written as

$$F_\lambda = \tau_\lambda^0(v_\lambda + \Delta_\lambda) \qquad (4)$$

The relaxation time of the mode obtained through perturbation theory is denoted as τ_λ^0 in the formula above, which is commonly utilized in the relaxation time approximation (RTA). Therefore, Δ_λ is a measure of the deviation of the total (and associated heat flux) of a particular phonon mode from the RTA prediction. Then, Δ_λ and τ_λ^0 can be computed as

$$\Delta_\lambda = \frac{1}{N}\sum_{\lambda'\lambda''}^{+} \Gamma_{\lambda\lambda'\lambda''}^{+}\left(\xi_{\lambda\lambda''}'' F_{\lambda''} - \xi_{\lambda\lambda'}F_{\lambda'}\right)$$
$$+ \frac{1}{N}\sum_{\lambda'\lambda''}\frac{1}{2}\Gamma_{\lambda\lambda'\lambda''}^{-}\left(\xi_{\lambda\lambda''}F_{\lambda''} + \xi_{\lambda\lambda'}F_{\lambda'}\right)$$
$$+ \frac{1}{N}\sum_{\lambda'}\Gamma_{\lambda\lambda'}\xi_{\lambda\lambda'}F_{\lambda'} \qquad (5)$$

$$\frac{1}{\tau_\lambda^0} = \frac{1}{N}\left(\sum_{\lambda'\lambda''}\Gamma_{\lambda\lambda'\lambda''}^{+} + \sum_{\lambda'\lambda''}\frac{1}{2}\Gamma_{\lambda\lambda'\lambda''}^{-} + \sum_{\lambda'}\Gamma_{\lambda\lambda'}\right) \qquad (6)$$

where $\xi_{\lambda\lambda'} = \frac{\omega_{\lambda'}}{\omega_\lambda}$. And the Brillouin zone is discretized into a regular grid of $N = N_1 \times N_2 \times N_3$ $\boldsymbol{q}$ points centered at Γ. Quasi-momentum conservation necessitates that

$\mathbf{q}'' = \mathbf{q} \pm \mathbf{q}' + \mathbf{Q}$ for some reciprocal vector $\mathbf{Q}$. Sum $\Sigma^{\pm}$, ensuring that the images of $\mathbf{q}''$, $\mathbf{q}$, and $\mathbf{q}'$ in the Brillouin zone are identical. The regularity of the sampling grid ensures that it also includes $\mathbf{q}''$. In equation (5), $\Gamma^{\pm}_{\lambda\lambda'\lambda''}$ represents the three-phonon scattering rate, which can be expressed as follows:

$$\Gamma^{+}_{\lambda\lambda'\lambda''} = \frac{\hbar\pi}{4} \frac{f_{\lambda'} - f_{\lambda''}}{\omega_{\lambda}\omega_{\lambda'}\omega_{\lambda''}} \left|V^{+}_{\lambda\lambda'\lambda''}\right|^2 \delta\left(\omega_{\lambda} + \omega_{\lambda'} - \omega_{\lambda''}\right) \quad (7)$$

$$\Gamma^{-}_{\lambda\lambda'\lambda''} = \frac{\hbar\pi}{4} \frac{f_{\lambda'} + f_{\lambda''} + 1}{\omega_{\lambda}\omega_{\lambda'}\omega_{\lambda''}} \left|V^{-}_{\lambda\lambda'\lambda''}\right|^2 \delta\left(\omega_{\lambda} - \omega_{\lambda'} - \omega_{\lambda''}\right) \quad (8)$$

Among them, $f_{\lambda'}$ is the abbreviation for $f(\omega_{\lambda'})$. The '+' sign corresponds to the phonon absorption process, while the '-' sign corresponds to the emission process. Energy conservation during the absorption and emission processes is represented by the Dirac distribution in the equation. Where $\Gamma^{\pm}_{\lambda\lambda'\lambda''}$ is the three phonon scattering rate corresponding to the absorption and emission processes, respectively. Here, λ, λ', and λ'' represent the modes of three phonons with corresponding quasi-momenta $\mathbf{q}$, $\mathbf{q}'$ and $\mathbf{q}''$ respectively.

These phonons adhere to the law of conservation of energy and momentum. By incorporating concepts such as phonon group velocity and phonon relaxation time, the lattice thermal conductivity κ_l is ultimately calculated as follows [41]:

$$\kappa_l = \frac{1}{NVk_BT^2} \sum_{\lambda} f^0_{\lambda}\left(f^0_{\lambda} + 1\right)\left(\hbar\omega_{\lambda}\right)^2 v^{\alpha}_{\lambda}v^{\beta}_{\lambda}\tau_{\lambda} \quad (9)$$

where N is the number of sampled q points in the Brillouin zone, and V is the volume of the unit cell. k_B is the Boltzmann constant. T is absolute temperature. f^0_{λ} is the equilibrium Boltzmann distribution depending on the phonon frequency. λ is phonon mode. And $\hbar$ represents Reduced Planck constant. ω_{λ} is the angular frequency. And v_{λ} represents the phonon group velocity, the indices α, β denote vector direction, and τ_{λ} denotes the phonon relaxation time (the reciprocal of the scattering rate). Conversely, the lattice thermal conductivity κ_l is negatively correlated with the Grüneisen parameter (γ), phase space, the number of scattering channels, and the phonon scattering rate. In this context, the ShengBTE software package is used to iteratively solve equation (4) starting from the zero-order approximation, where $F^0_{\lambda} = \tau^0_{\lambda}v_{\lambda}$. Ultimately, the exact solution for κ_l is obtained.

As shown in Figure 4, the variation of thermal conductivity values of MAlB with different grid densities during the solution process of the BTE. The inset illustrates the thermal conductivity of WAlB for clarity. The results indicate that when the grid density in all three dimensions is
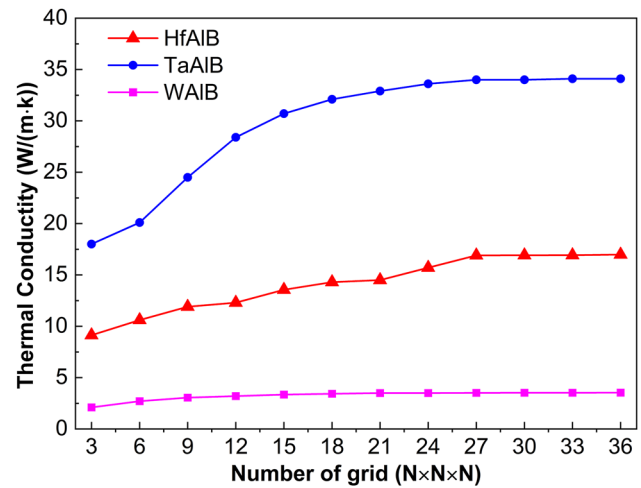

Figure 4: Convergence test for mesh density.

$N \times N \times N \geq 27 \times 27 \times 27$, the fluctuation in thermal conductivity remains stable within 3 %. To ensure calculation accuracy, this paper selects a grid density of $35 \times 35 \times 35$. And the final result can be compared to similar materials found in the reference [42].

3.4.1 Thermal conductivity

There is a physical relationship between $\frac{1}{\tau^{ph}_{\lambda}}$, W (or P_3), and γ along with the phonon group velocity (v_{λ}) and the phonon relaxation time (τ_{λ}) which are the primary determinants of the lattice's thermal conductivity [36, 43, 44]. Finally, the lattice thermal conductivity (as shown in equation (9)) has been obtained.

Figure 5 illustrates the cumulative variation trend of lattice thermal conductivity in relation to the phonon mean free path (MFP) for HfAlB, TaAlB, and WAlB at a temperature of 300 K. Material size is a critical factor influencing lattice thermal conductivity. For these three materials – HfAlB, TaAlB, and WAlB – when the phonon mean free paths exceed 231.0 nm, 278.3 nm, and 2,595.0 nm, respectively, their lattice thermal conductivity remain constant. This phenomenon indicates that the phonons primarily responsible for heat conduction have mean free paths that are smaller than the corresponding critical dimensions. When the material sizes exceed these critical dimensions (231.0 nm, 278.3 nm, and 2,595.0 nm), the lattice thermal conductivity of HfAlB, TaAlB, and WAlB show minimal changes, with almost no observable phonon scattering, leading to a stabilization of the lattice thermal conductivity. Ultimately, the lattice thermal conductivity of HfAlB, TaAlB, and WAlB stabilize at 16.9 W/(m K), 34.0 W/(m K), and 3.5 W/(m K), respectively.
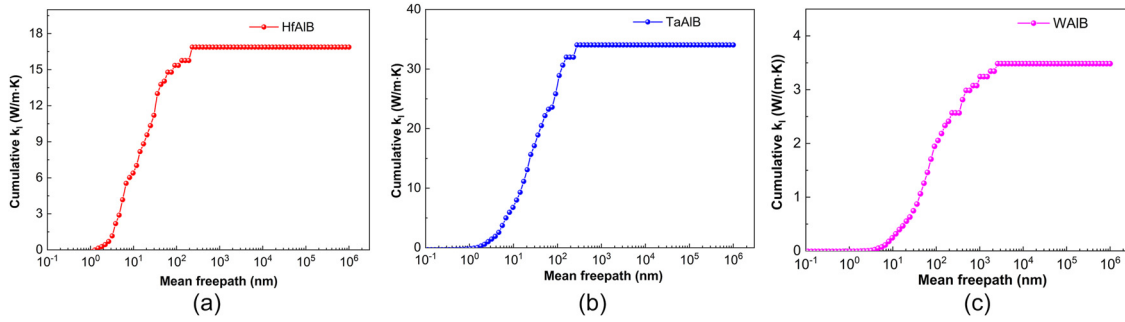
Figure 5: Lattice thermal conductivity of HfAlB (a), TaAlB (b), WAlB (c).

3.4.2 Phonon relaxation time

The phonon relaxation time τ_λ is determined by the reciprocal of the anharmonic scattering rate of three phonons, while $\frac{1}{\tau_\lambda}$ is influenced by disordered two-phonon scattering and the anharmonic scattering of three phonons. It is equal to the sum of the three-phonon anharmonic scattering rate $\frac{1}{\tau_\lambda^{anh}}$ and the two-phonon isotope scattering rate $\frac{1}{\tau_\lambda^{iso}}$. The value of $\frac{1}{\tau_\lambda^{anh}}$ can be determined as the sum of the three-phonon transition probabilities $\Gamma_{\lambda\pm\lambda'\lambda''}^{\pm}$. And

$$\frac{1}{\tau_\lambda^{ph}} = \frac{1}{\tau_\lambda^{anh}} + \frac{1}{\tau_\lambda^{iso}} \tag{10}$$

where $\frac{1}{\tau_\lambda^{ph}}$, $\frac{1}{\tau_\lambda^{anh}}$, and $\frac{1}{\tau_\lambda^{iso}}$ represent the total scattering rate, the anharmonic three-phonon scattering rate, and the isotope scattering rate, respectively.

As shown in Figure 6(a)–(c), the results demonstrate the variation of relaxation times with frequency for HfAlB, TaAlB, and WAlB at 300 K. In Figure 6(a), it is evident that the relaxation times of the acoustic branches for HfAlB are greater than those of the optical branches. Notably, the LA mode displays the longest relaxation time of 185.6 ps. The phonon relaxation times for the TA_1 and TA_2 modes are relatively short, all measuring below 68.1 ps. Within the frequency range of 3.1–25.1 THz, the phonon relaxation times

are primarily influenced by the optical branches, with all values remaining below 21.4 ps.

It can be observed from Figure 6(b) that TaAlB exhibits shorter relaxation times compared to HfAlB. In TaAlB, the relaxation times associated with the majority of its acoustic branches are longer than those of its optical branches, with only a small fraction of the optical branches attaining significantly high relaxation times. Specifically, the relaxation time for the LA mode of TaAlB is less than 130.9 ps. The phonon relaxation times for both the TA_1 and TA_2 modes are relatively large, remaining below 152.3 ps. Within the frequency range of 3.4–23.6 THz, the phonon relaxation times of TaAlB are primarily influenced by its optical branches, all of which stay below the maximum value of 49.7 ps.

It can be observed from Figure 6(c) that WAlB exhibits significantly shorter relaxation times compared to both HfAlB and TaAlB. For WAlB, the relaxation times for most of its acoustic branches are comparable to those of its low optical branches, with only a few acoustic branches reaching notably high values. Specifically, the relaxation time for the TA_1 mode of WAlB is below 77.6 ps. The phonon relaxation times for both the TA_2 and LA modes are relatively short, remaining below 57.5 ps. Within the frequency range of 3.4–21.6 THz, the phonon relaxation times of WAlB are primarily influenced by its optical branches, all of which remain below the peak value of 59.5 ps.
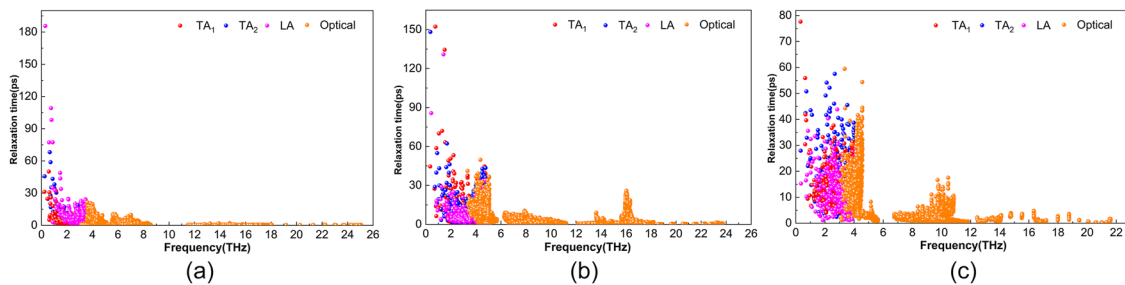

Figure 6: Phonon relaxation time of HfAlB (a), TaAlB (b), WAlB (c).

At 300 K, the TA_1, TA_2, LA, and optical phonons of HfAlB, TaAlB, and WAlB all demonstrate relatively high relaxation times. The extended phonon relaxation times suggest that phonons significantly contribute to the thermal transport process over longer durations. As a result, this enhances the lattice thermal conductivity. On the whole, although mid-to-high frequency optical phonon modes contribute to thermal transport, the lattice thermal conductivity is primarily dominated by contributions from acoustic phonon modes and low-frequency optical modes. As shown in the figures, the relaxation times for HfAlB, TaAlB, and WAlB generally follow the trend of $\tau_{HfAlB} > \tau_{TaAlB} > \tau_{WAlB}$. However, this trend does not completely align with the conclusions drawn from their thermal conductivity patterns.

3.4.3 Phonon group velocity

The phonon group velocity v is the derivative of frequency with respect to the wave vector, which is a crucial factor in evaluating heat transport capacity. The phonon group velocity can be calculated from the trend of the phonon dispersion [45].

As shown in Figure 7, the phonon group velocities of HfAlB, TaAlB, and WAlB are quite similar. In Figure 7(a), the acoustic branches TA_1, TA_2, and LA of HfAlB exhibit low group velocities, predominantly concentrated near 2 THz. Among these, the TA_2 mode shows the lowest phonon group velocity, with a peak value of approximately 0.38 km/s. In the low-frequency domain, the LA mode exhibits the highest group velocity, with certain phonons reaching speeds of up to 0.46 km/s. Meanwhile, a limited number of phonons in the TA_1 mode achieve group velocities of approximately 0.41 km/s. Optical phonons within the frequency range of 3.1–8.6 THz have group velocities lower than those of acoustic phonons, with a maximum value of 0.26 km/s. In contrast, optical branches in the high-frequency region, spanning 11.5 to 25.1 THz, exhibit higher group velocities, reaching a maximum of 0.62 km/s.

As shown in Figure 7(b) for TaAlB, the acoustic branches TA_1, TA_2, and LA exhibit slightly elevated group velocities,

with most velocities concentrated around 2.5 THz. Among these, the LA mode has the highest phonon group velocity, reaching approximately 0.49 km/s. In the low-frequency region, several phonons in the TA_1 mode achieve a group velocity of 0.39 km/s, and a similar velocity is observed for a small fraction of phonons in the TA_2 mode, closely approaching the maximum value of the TA_1 mode. The optical phonons near 4.3 THz exhibit group velocities of 4.3 km/s, which are lower than those of the acoustic phonons. Within the frequency range of 6.3–11.2 THz, the group velocities of certain optical branches reach a partial maximum of 0.21 km/s. In contrast, the optical branches in the high-frequency region, from 12.1 to 23.7 THz, attain a significantly higher maximum group velocity of 0.49 km/s.

As depicted in Figure 7(c), WAlB generally exhibits lower phonon group velocities compared to HfAlB and TaAlB. The group velocities of the TA_1, TA_2, and LA modes in WAlB are comparable to those of the high-frequency optical branches, predominantly clustered around 2.6 THz. Among these modes, the LA mode shows the highest phonon group velocity, reaching a maximum value of approximately 0.41 km/s. In the low-frequency region, the TA_1 mode displays a relatively slow group velocity, with only a limited number of phonons achieving a velocity of 0.37 km/s. A similar group velocity, approximately 0.39 km/s, is observed for a small fraction of phonons in the TA_2 mode. The group velocities of the optical branches within the frequency range of 3.2–5.6 THz are notably low, with a maximum value of only 0.21 km/s. As the frequency range shifts to 6.8 to 11.8 THz, the group velocities of the optical phonons increase slightly, reaching a maximum of 0.22 km/s. In contrast, the optical branches in the high-frequency region, spanning 12.5 to 21.6 THz, exhibit significantly higher group velocities, peaking at 0.45 km/s. This variation in group velocities across different frequency ranges provides valuable insights into the dynamic behavior of optical phonons in the material.

Overall, the relationship among the phonon group velocities associated with the TA_1, TA_2, and LA modes of the three materials is as follows: $v_{TaAlB} > v_{HfAlB} > v_{WAlB}$.
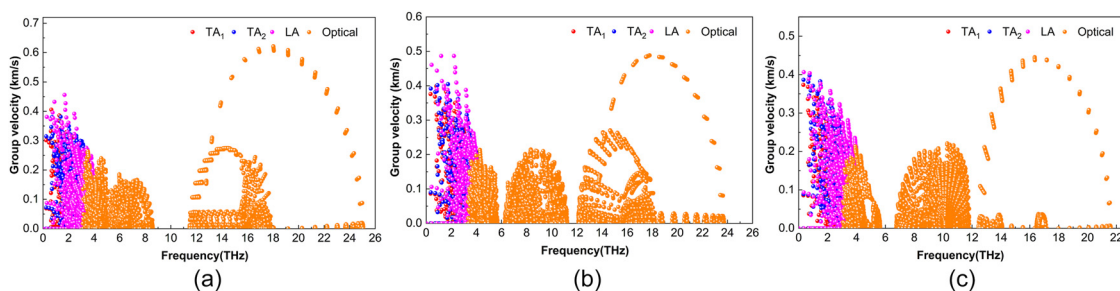

Figure 7: Phonon group velocity of HfAlB (a), TaAlB (b), WAlB (c).

The results align with the experimental findings concerning their thermal conductivity.

3.4.4 Grüneisen parameter

In equations (7) and (8), $V_{\lambda\lambda'\lambda''}^{\pm}$ represents the scattering matrix element.

$$V_{\lambda\lambda'\lambda''}^{\pm} = \sum_{i\in u\cdot c}\sum_{jl}\sum_{kl'}\sum_{\alpha\beta\gamma}\Phi_{i\alpha,j\beta,k\gamma}(0,l,l')e^{i\mathbf{q}'\cdot\mathbf{R}_l}e^{i\mathbf{q}''\cdot\mathbf{R}_l'}$$

$$\times\frac{e_{i\alpha}^{\lambda}e_{j\beta}^{\pm\lambda'}e_{k\gamma}^{-\lambda''}}{\sqrt{M_iM_jM_k}} \tag{11}$$

Here, i, j, and k are atomic indices, while α, β, and γ denote Cartesian coordinates. In the summation process, i runs only over the atoms in the central unit cell, while j and k cover the entire system. $-\lambda''$ is the abbreviated form of $\mathbf{q}$ and $\mathbf{R}$. M_i represents the mass of the i-th atom. $e_{i\alpha}^{\lambda}$ denotes the α component of the harmonic eigenvector of mode λ at atom i. $0, l, l'$ and denote coordinate indices referring to the reference unit cell 0, the unit cell l, l' adjacent to 0. The range of l, l' is determined by the number of primitive cells contained within the supercell defined during the calculation. The mode Grüneisen parameter γ, in the anharmonic approximation, is defined as

$$\gamma_\lambda = \frac{-1}{6\omega_\lambda^2}\sum_{i\in u\cdot c}\sum_{jl}\sum_{kl'}\sum_{\alpha\beta\gamma}\Phi_{i\alpha,j\beta,k\gamma}(0,l,l')\times\frac{e_{i\alpha}^{\lambda*}\cdot e_{j\beta}^{\lambda}}{\sqrt{M_iM_j}}$$

$$\times e^{\mathbf{q}\cdot\mathbf{R}_l}\mathbf{r}_{l'k\gamma} \tag{12}$$

where $\Phi_{i\alpha,j\beta,k\gamma}(0,l,l')$ is 3rd-order IFC,

$$\Phi_{i\alpha,\beta,k\gamma}(0,l,l') = \frac{\partial^3 E_{tot}}{\partial u_{i\alpha}^0\partial u_{j\beta}^l\partial u_{k\gamma}^{l'}} \tag{13}$$

where k is the atomic index in unit cell l'. At the same time, the strength of the interaction is typically determined by the anharmonicity interaction, which is characterized by the Grüneisen parameter (γ). This means the greater the anharmonicity, the stronger the phonon-phonon interaction, and the lower the thermal conductivity of the lattice.

Figure 8(a)–(c) illustrate the γ parameters for various phonon modes of the HfAlB, TaAlB, and WAlB materials, respectively. Both the acoustic and optical phonons of HfAlB and TaAlB exhibit relatively low absolute values of γ. In contrast, WAlB demonstrates a significantly higher absolute value of γ. For HfAlB and TaAlB, the highest absolute values of γ, approximately 10.1 and 4.9, are associated with the TA$_1$ and LA mode respectively. This indicates that these two compounds exhibit relatively weaker anharmonicity compared to WAlB. Additionally, the absolute value of γ in the optical mode is slightly lower for HfAlB, reaching a maximum of 1.38, while for TaAlB, it is comparatively lower in the optical mode, with a peak value of 2.43.

In contrast, the WAlB material demonstrates an exceptionally high maximum absolute value of γ, reaching 19.96, which is associated with the TA$_1$ mode. The absolute values of γ for the TA$_2$ and LA modes are relatively smaller, ranging from 0 to 4.1 THz, with maximum values of 18.98 and 18.57, respectively. For the optical branches distributed within the frequency range of 3.2 THz to 21.6 THz, the maximum absolute value of γ is 8.79, indicating significant anharmonicity in WAlB. Furthermore, there is an overlap between the acoustic and optical branches in WAlB, which corresponds to the phonon dispersion diagram presented earlier. This overlap also suggests potential crossings between the acoustic and optical branches, which may lead to increased scattering and a possible reduction in lattice thermal conductivity.

The pronounced peaks observed in WAlB are likely attributed to stronger anharmonic vibrations of atoms within its lattice, which lead to intense phonon-phonon scattering and, consequently, high anharmonicity. WAlB exhibits particularly strong anharmonicity, enhancing phonon scattering and thereby reducing the thermal conductivity of the WAlB compound. In contrast, HfAlB and TaAlB exhibit the opposite behavior, as their relatively lower anharmonicity contributes to higher thermal conductivity. Notably, the distribution of γ values in TaAlB
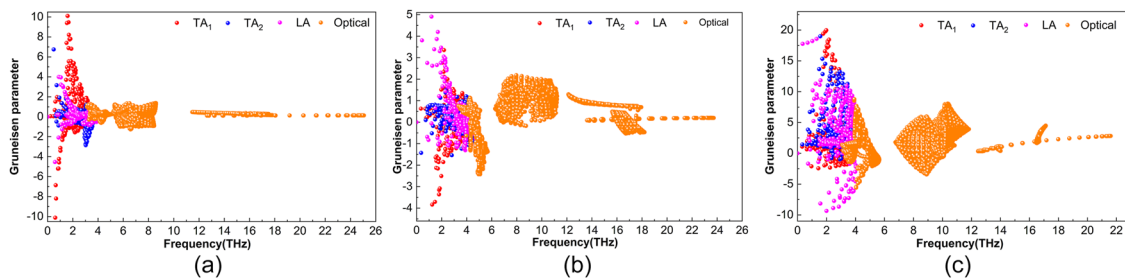

Figure 8: Grüneisen parameter of HfAlB (a), TaAlB (b), WAlB (c).

appears more dispersed. Furthermore, the high $|\gamma|$ values in WAlB are primarily attributed to low-frequency acoustic branches, which significantly hinder heat conduction, leading to even lower thermal conductivity. The presence of negative γ values in HfAlB, TaAlB, and WAlB indicates the potential for negative thermal expansion in these materials. In summary, the relationship among the absolute values of γ for HfAlB, TaAlB, and WAlB can be expressed as follows: $|\gamma_{\text{WAlB}}| > |\gamma_{\text{HfAlB}}| > |\gamma_{\text{TaAlB}}|$.

In general, when examining the Grüneisen parameters (γ) of the MAlB compounds, the relationship is as follows: $|\gamma_{\text{WAlB}}| > |\gamma_{\text{HfAlB}}| > |\gamma_{\text{TaAlB}}|$, with $|\gamma_{\text{WAlB}}|$ being significantly larger than both $|\gamma_{\text{HfAlB}}|$ and $|\gamma_{\text{TaAlB}}|$. This trend partially aligns with the conclusions drawn from thermal conductivity measurements. Interestingly, $|\gamma_{\text{HfAlB}}|$ is greater than $|\gamma_{\text{TaAlB}}|$, then the lattice thermal conductivity of HfAlB is lower than that of TaAlB. This observation contradicts the assumption that lattice thermal conductivity would decrease sequentially according to the order of the metal M elements in the periodic table (Hf, Ta, W). This observation suggests a potential antagonistic relationship among the Grüneisen parameter, phonon relaxation time, and phonon group velocity. For the three materials – HfAlB, TaAlB, and WAlB – the Grüneisen parameter appears to be a dominant factor influencing their lattice thermal conductivity, although phonon relaxation time and group velocity also contribute to some extent. Based on the thermal conductivity data, TaAlB and HfAlB may be more suitable for thermal conduction applications, whereas WAlB, with its lower thermal conductivity, is better suited for thermal barrier coating materials.

3.4.5 Variation of lattice thermal conductivity with temperature

The variation in lattice thermal conductivity of HfAlB, TaAlB, and WAlB with temperature is shown in Figure 9. Specifically, at 200 K, the thermal conductivity values for HfAlB, TaAlB, and WAlB are 24.4 W/(m K), 52.0 W/(m K), and 5.7 W/(m K), respectively. In contrast, when the temperature increases to 950 K, these values decrease to 13.7 W/(m K), 6.1 W/(m K), and 1.1 W/(m K), respectively. Analysis of the thermal conductivity data reveals a consistent trend: as temperature increases, the lattice thermal conductivity of HfAlB, TaAlB, and WAlB initially decreases gradually and eventually stabilizes. This behavior can be attributed to the following mechanism: elevated temperatures induce more intense lattice vibrations, which increase the likelihood of phonon-phonon scattering and the frequency of phonon collisions. Additionally, anharmonic effects within the
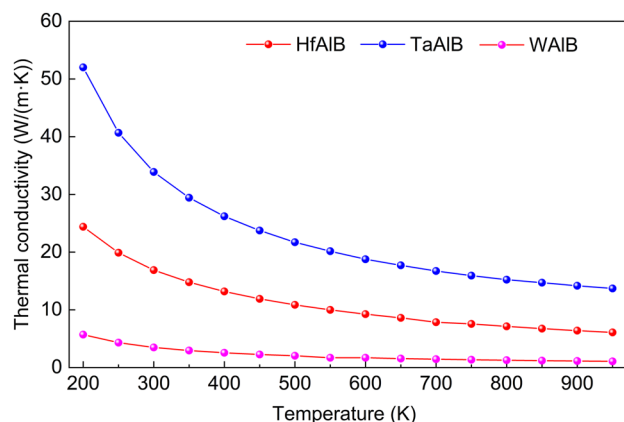

Figure 9: The variation of lattice thermal conductivity in HfAlB, TaAlB, and WAlB with temperature.

materials are enhanced at higher temperatures. Together, these factors cause the thermal conductivity curve to gradually flatten.

4 Infrared and Raman spectra

The phonon vibrational frequencies via DFPT method [46]. The infrared intensity of a phonon eigenmode is given by the square of the scalar product between the Born effective charge tensor and the normalized eigenvector, as defined in equation:

$$I_{\text{IR}}(s) = \sum_{\alpha} \left| \sum_{j} \sum_{\beta} Z_{\alpha\beta}^* X_{\beta}(s, j) \right|^2 \tag{14}$$

where $Z_{\alpha\beta}^*$ is the Born effective charge tensor component. $X_{\beta}(s, j)$ represents the normalized vibrational eigenvector of the jth phonon mode of the sth atom in the unit cell. And the long-range behavior of the Coulomb interaction generates a macroscopic electric field, which causes mutual coupling between phonon modes. This electric field leads to the splitting of phonons into the transverse optical (TO) and longitudinal optical (LO) modes at the Γ-point. The effective charge tensor of Born is a crucial parameter that determines the LO/TO splitting phenomenon. Raman activity tensors of an eigenmode are evaluated by taking the derivative of the high-frequency macroscopic dielectric constant ε^∞ with respect to the normal mode amplitude $Q(s)$ using a central difference scheme and the Raman intensities are then defined as [47, 48]:

$$I_{\text{Raman}} = 45 \left| \frac{1}{3} \left(I_{11} + I_{22} + I_{33} \right) \right|^2 + \frac{7}{2} \Big[\left(I_{11} - I_{22} \right)^2 \\ + \left(I_{11} - I_{33} \right)^2 + \left(I_{22} - I_{33} \right)^2$$

$$+ 6\left(I_{12}^2 + I_{13}^2 + I_{23}^2\right)\big] \tag{15}$$

In equation (15), the $I_{\alpha\beta}$ was used in place of $I_{\mathrm{Raman},\alpha\beta}(s)$ [49, 50]. Theoretically, HfAlB, TaAlB, and WAlB each possess a total of 18 vibrational modes at the center of the Brillouin zone. The irreducible representations of their vibrational modes at the Γ point are as follows:

$$M = 3A_g + 3B_{1g} + 3B_{1u} + 3B_{2u} + 3B_{3g} + 3B_{3u} \tag{16}$$

There are three types of irreducible representations for the acoustic branches, corresponding to three lattice waves:

$$\Gamma_{\mathrm{acoustic}} = B_{1u} + B_{2u} + B_{3u} \tag{17}$$

There are 15 irreducible representations for the optical branches, corresponding to 15 lattice waves.

$$\Gamma_{\mathrm{optic}} = 3A_g + 3B_{1g} + 2B_{1u} + 2B_{2u} + 3B_{3g} + 2B_{3u} \tag{18}$$

Based on the character tables of the point groups, it can be observed that among the optical modes of HfAlB, TaAlB, and WAlB, there are a total of six infrared-active modes: $2B_{1u} + 2B_{2u} + 2B_{3u}$. Additionally, there are nine Raman-active modes: $3A_g + 3B_{1g} + 3B_{3g}$. Following structural optimization, we calculated the phonon dispersion and infrared/Raman

spectra of the ternary borides HfAlB, TaAlB, and WAlB, as shown in Figures 10 and 11.

4.1 Infrared spectra

Figure 10(a) illustrates the positions and vibration intensities of the six infrared vibrational mode peaks for the HfAlB material. Among these, the modes at 184.1 cm^{-1}(B$_{3u}$) and 195.9 cm^{-1}(B$_{2u}$) in the HfAlB structure exhibit strong infrared vibration intensities and are easily distinguishable. The modes at 195.9 cm^{-1}(B$_{2u}$), 396.6 cm^{-1}(B$_{2u}$), and 521.8 cm^{-1}(B$_{3u}$) display lower infrared vibration intensities but can still be clearly identified. The mode at 420.9 cm^{-1}(B$_{1u}$) exhibits a relatively low infrared vibrational intensity, necessitating careful observation for accurate identification. Furthermore, the infrared peak of the 183.9 cm^{-1}(B$_{1u}$) mode is very close to that of the 184.1 cm^{-1}(B$_{3u}$) mode, rendering them nearly indistinguishable from one another.

Figure 10(b) illustrates the positions and vibration intensities of the six infrared vibrational mode peaks for the TaAlB material. Among these modes in the TaAlB structure, those at 208.7 cm^{-1}(B$_{1u}$), 212.0 cm^{-1}(B$_{3u}$), and 268.9 cm^{-1}(B$_{2u}$) demonstrate strong infrared vibration intensities and are easily identifiable. In contrast, the modes
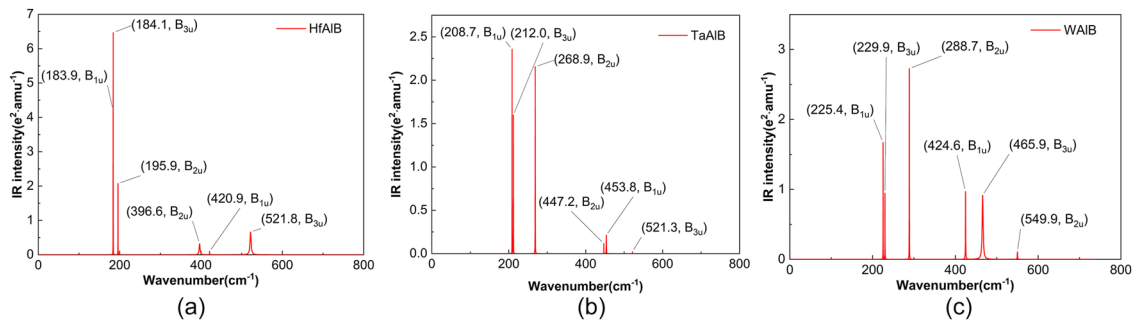

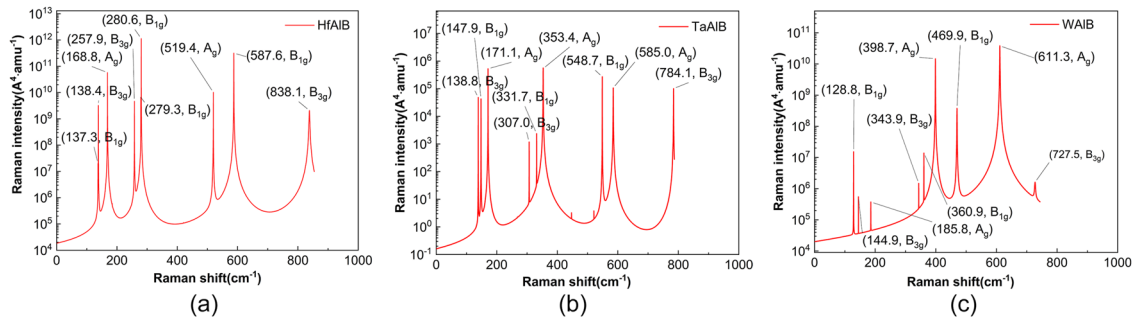**Figure 10:** Infrared spectra of HfAlB (a), TaAlB (b), WAlB (c).

Figure 11: Raman spectra of HfAlB (a), TaAlB (b), WAlB (c).

at 447.2 cm^{-1}(B$_{2u}$), 453.8 cm^{-1}(B$_{1u}$), and 521.3 cm^{-1}(B$_{3u}$) exhibit lower infrared vibrational intensities, yet they remain distinguishable. The peaks at 208.7 cm^{-1}(B$_{1u}$) and 212.0 cm^{-1}(B$_{3u}$) are closely spaced, requiring careful discrimination to differentiate between them.

Figure 10(c) illustrates the positions and vibration intensities of the six infrared vibrational mode peaks for the WAlB material. Among these modes in the WAlB structure, those at 225.4 cm^{-1}(B$_{1u}$), and 288.7 cm^{-1}(B$_{2u}$) demonstrate relatively strong infrared vibration intensities and are comparatively easier to identify. The modes at 229.9 cm^{-1}(B$_{3u}$), 424.6 cm^{-1}(B$_{1u}$), and 465.9 cm^{-1}(B$_{3u}$) exhibit lower infrared vibrational intensities but are still identifiable. The mode at 549.9 cm^{-1}(B$_{2u}$) also presents a low infrared vibrational intensity, requiring careful observation for accurate identification. Notably, the infrared peak of the 225.4 cm^{-1}(B$_{1u}$) mode is very close to that of the 229.9 cm^{-1}(B$_{3u}$) mode, necessitating meticulous scrutiny and confirmation to differentiate between the two peaks.

From a structural perspective, MAlB exhibits a layered architecture, consisting of alternating metal layers (M/Al) and boron layers. Within this structure, the boron atoms can form chain-like or two-dimensional network configurations. In terms of vibrational characteristics, low-frequency vibrations are primarily induced by interlayer shearing or out-of-plane vibrations of the metal M atomic layers, with these vibrational modes predominantly influenced by metallic bonding interactions. Mid- to high-frequency vibrations are significantly contributed to by the vibrations of M atoms, Al atoms, and B atoms. These vibrations may arise from weak metal-boron interactions between M/Al and B, such as lateral vibrations of M-B/Al−B bonds, or from in-plane bending and torsional vibrations of boron chains. Within the mid-frequency range, these vibrations exhibit coupling effects. The high-frequency vibrations primarily originate from the movements of B atoms, especially those related to the stretching of the strong covalent bonds between B−B atoms.

4.2 Raman spectra

As shown in Figure 11(a), the HfAlB material exhibits nine Raman-active modes at specific frequencies: 137.3 cm^{-1}(B$_{1g}$), 138.4 cm^{-1}(B$_{3g}$), 168.8 cm^{-1}(A$_g$), 257.9 cm^{-1}(B$_{3g}$), 279.3 cm^{-1}(B$_{1g}$), 280.6 cm^{-1}(B$_{1g}$), 519.4 cm^{-1}(A$_g$), 587.6 cm^{-1}(B$_{1g}$), and 838.1 cm^{-1}(B$_{3g}$). Figure 10(a) presents the detailed peak positions and intensities of the Raman vibrational modes. Among these modes, the cases where 137.3 cm^{-1}(B$_{1g}$) is very close to 138.4 cm^{-1}(B$_{3g}$) and 279.3 cm^{-1}(B$_{1g}$) is near 280.6 cm^{-1}(B$_{1g}$) result in mutual masking, making these particular modes difficult to distinguish. In contrast, the other modes exhibit relatively high vibrational intensities and are easily identifiable.

As shown in Figure 11(b), the TaAlB material exhibits nine Raman-active modes at the following frequencies: 138.8 cm^{-1}(B$_{3g}$), 147.9 cm^{-1}(B$_{1g}$), 171.1 cm^{-1}(Ag), 307.0 cm^{-1}(B$_{3g}$), 331.7 cm^{-1}(B$_{1g}$), 353.4 cm^{-1}(Ag), 548.7 cm^{-1}(B$_{1g}$), 585.0 cm^{-1}(Ag), and 784.1 cm^{-1}(B$_{3g}$). Figure 10(b) presents the detailed peak positions and intensities of the Raman vibrational modes. Among these modes, the peaks at 138.8 cm^{-1}(B$_{3g}$) and 147.9 cm^{-1}(B$_{1g}$) are in close proximity, necessitating careful discrimination to differentiate between them. All nine Raman modes of the TaAlB material exhibit relatively high vibrational intensities and are easily distinguishable. As illustrated in Figure 10(b), the Raman spectrum also reveals several "spikes" (minor peaks) that may only become apparent or identifiable with advanced Raman spectroscopy equipment.

As shown in Figure 11(c), the WAlB material exhibits nine Raman-active modes at the following frequencies: 128.8 cm^{-1}(B$_{1g}$), 144.9 cm^{-1}(B$_{3g}$), 185.8 cm^{-1}(A$_g$), 343.9 cm^{-1}(B$_{3g}$), 360.9 cm^{-1}(B$_{1g}$), 398.7 cm^{-1}(A$_g$), 469.9 cm^{-1}(B$_{1g}$), 611.3 cm^{-1}(A$_g$), and 727.5 cm^{-1}(B$_{3g}$). Figure 10(c) illustrates the specific peak positions and intensities of the Raman vibrational modes. Among these modes, the peaks at 128.8 cm^{-1}(B$_{1g}$), 398.7 cm^{-1}(A$_g$), 469.9 cm^{-1}(B$_{1g}$), and 611.3 cm^{-1}(A$_g$) are easily distinguishable due to their relatively high intensities. The peaks at 144.9 cm^{-1}(B$_{3g}$), 185.8 cm^{-1}(A$_g$), 343.9 cm^{-1}(B$_{3g}$), and 360.9 cm^{-1}(B$_{1g}$) are relatively weak, but they can still be accurately distinguished. Although the peak at 727.5 cm^{-1}(B$_{3g}$) has a lower intensity, it remains identifiable because it is sufficiently separated from the other peaks.

From a holistic perspective, there is a notable similarity between Raman spectra and infrared (IR) spectra. The presence of lower vibrational frequencies can primarily be attributed to the relatively large masses of the metal M and Al atoms, as well as the bending vibrations of M−Al bonds. In the mid-frequency range, it is hypothesized that these vibrations may arise from interactions between the metallic M layers and the boron layers, or from the in-plane bending and torsional vibrations of B−B chains. On the other hand, high-frequency vibrations are likely associated with the stretching vibrations of strong covalent bonds between B atoms, as well as the coupled vibrations of Al and B atoms. In high-frequency vibrations, the contributions from the vibrations of metal M atoms and Al atoms are relatively minor. This may be due to the strength of the M−B bonds and the relatively low mass of the B atoms, which results in these stretching vibration modes exhibiting higher vibrational frequencies.

Through the Raman spectroscopic analysis of HfAlB, TaAlB, and WAlB materials, we can derive characteristics closely related to lattice vibrational properties (phonon behavior). These characteristics can indirectly reflect the influence of phonon transport efficiency, scattering mechanisms, and lattice dynamics on the thermal conductivity of HfAlB, TaAlB, and WAlB materials. The Raman spectra of HfAlB and TaAlB materials display a series of sharp low-frequency phonon peaks at 137.3 cm^{-1}(B_{1g}), 138.4 cm^{-1}(B_{3g}), 168.8 cm^{-1}(A_g) of HfAlB and 138.8 cm^{-1}(B_{3g}), 147.9 cm^{-1}(B_{1g}), 171.1 cm^{-1}(A_g) of TaAlB, all exhibiting relatively high vibrational intensities. This observation suggests that phonons encounter minimal scattering as they propagate through the HfAlB and TaAlB lattices, which facilitates thermal conduction and contributes to the attainment of higher lattice thermal conductivity. In contrast, the Raman spectrum of the WAlB material exhibits low-frequency peaks at 128.8 cm^{-1}(B_{1g}), 144.9 cm^{-1}(B_{3g}), and 185.8 cm^{-1}(A_g), each with significant vibrational intensities. This finding reflects the low thermal conductivity of WAlB and illustrates the strong connection between Raman spectroscopy and thermal conductivity.

5 Conclusions

The study reveals that HfAlB, TaAlB, and WAlB are layered ternary borides belonging to the *Cmcm* space group, exhibiting metallic properties. Their performance is influenced by a combination of M−B covalent bonds, metallic bonds within the aluminum layers, and interlayer ionic bonds. phonon dispersion indicate that these materials are dynamically stable, with boron atoms primarily contributing to high-frequency vibrations, while M/Al atoms predominantly govern low-frequency vibrations. Additionally, lattice thermal conductivity is significantly affected by anharmonicity. TaAlB (34.0 W/(m K)) and HfAlB (16.9 W/(m K)) exhibit high thermal conductivity due to their weak anharmonicity and long phonon relaxation times. In contrast, WAlB (3.5 W/(m K)) shows significant phonon scattering as a result of strong anharmonicity, which leads to its lower thermal conductivity. In the Raman spectra, each of the three materials displays nine active modes. The low-frequency modes correspond to M/Al vibrations, while the high-frequency modes are associated with the covalent bonds of B atoms. The presence of strong low-frequency peaks in HfAlB and TaAlB indicates minimal phonon scattering, which is consistent with their thermal conductivity results. This research offers theoretical guidance for the application of MAlB materials in high-temperature structural

components, electronic thermal management, and thermal barrier coatings.

Author contributions: Shengzhao Wang: investigation (equal); methodology (equal); project administration (equal); writing – original draft (equal); writing – review and editing (equal). Jinfan Song: conceptualization (equal); data curation (equal). Bin Liu: formal analysis (equal); Investigation (equal). All authors have accepted responsibility for the entire content of this manuscript and approved its submission.

Conflict of interest: The authors state no conflict of interest.
Data availability statement: The data that support the findings of this study are available from the corresponding author upon reasonable request.

References

1. Potanin AY, Bashkirov EA, Karpenkov AY, Levashov EA. Fabrication of high-strength magnetocaloric Fe_2AlB_2 MAB phase ceramics via combustion synthesis and hot pressing. Materialia 2024;33: 101993.

2. Wang Z, Qin S, Gao J, Mao J, Wang M, Xin B, et al. Microstructure evolution of MAB-phase WAlB during helium irradiation and post-irradiation annealing. Ceram Int 2025;51:1674−81.

3. Zhang Y, Zhang G, Wang T, Wang C, Xie Z, Wang W, et al. Synthesis, microstructure and properties of MoAlB MAB phase films. Ceram Int 2023;49:23714−20.

4. Samanta B, Dilanga Siriwardane EM, Çakır D. *Ab initio* prediction of phase stability of quaternary $Mo_{1−x}M_x$AlB (M = Cr, Fe, Mn, Nb, Sc, Ta, Ti, V, and W) MAB solid solutions. J Appl Phys 2024;136: 065104.

5. Lu Z, Qi X, He X, Zhang J, Fan Y, Yin H, et al. Lattice dynamics, Raman and IR vibrations of stable Al/Si-containing MAB phases: an ab initio and experimental study. J Am Ceram Soc 2024;107:6853−67.

6. Rezaie AA, Yan Z, Scheifers JP, Zhang J, Guo J, Fokwa BPT. Synthesis and Li-ion electrode properties of layered MAB phases $Ni_{n+1}ZnB_n$ (*n* = 1, 2). J Mater Chem A 2020;8:1646−51.

7. Zhang D, Richardson P, Wang M, He L, Shi L, Gao J. Experimental and theoretical investigation of the damage evolution of irradiated MoAlB and WAlB MAB phases. J Alloys Compd 2023;942:169099.

8. Muhammad Z, Usman M, Ullah S, Zhang B, Lu Q, Zhu L, et al. Lattice dynamics, optical and thermal properties of quasi-two-dimensional anisotropic layered semimetal $ZrTe_2$. Inorg Chem Front 2021;8:3885−92.

9. Zhang X, Zhou J, Fu W, Chen L. Research on materials of solar selective absorption coating based on the first principle. Open Phys 2021;19:477−85.

10. Akande SO, Samanta B, Sevik C, Cakir D. First-principles investigation of mechanical and thermal properties of MAlB (M = Mo, W), Cr_2AlB_2, and Ti_2InB_2. Phys Rev Appl 2023;20:044064.

11. Wang C, Wang H, Chen YB, Yao S-H, Zhou J. First-principles study of lattice thermal conductivity in $ZrTe_5$ and $HfTe_5$. J Appl Phys 2018;123:175104.

12. Muthaiah R, Tarannum F, Annam RS, Nayal AS, Danayat S, Garg J. Thermal conductivity of hexagonal BC_2P − a first-principles study. RSC Adv 2020;10:42628−32.

13. Liu G, Sun HY, Zhou J, Li QF, Wan X-G. First-principles study of lattice thermal conductivity of Td−WTe_2. New J Phys 2016;18:033017.

14. Ren Q, Li Y, Lun Y, Tang G, Hong J. First-principles study of the lattice thermal conductivity of the nitride perovskite $LaWN_3$. Phys Rev B 2023;107:125206.

15. Peng Q, Yuan X, Zhao S, Chen X-J. Lattice thermal conductivity of $Mg_3(Bi,Sb)_2$ nanocomposites: a first-principles study. Nanomaterials 2023;13:2938.

16. Kirtley J, Leichner V, Anderson BR, Eilers H. A comparison of pulsed and continuous lasers for high-temperature Raman measurements of anhydrite. J Raman Spectrosc 2018;49:862−71.

17. Song D, Ryu M, Pyeon J, Jeon H-B, Song T, Paik U, et al. Phase-reassembled high-entropy fluorites for advanced thermal barrier materials. J Mater Res Technol 2023;23:2740−9.

18. Liu F, Wei Z, Hu X, Cai Y, Chen Z, Yang C, et al. Asymmetric segregated network design of ultralight and thermal insulating polymer composite foams for green electromagnetic interference shielding. Compos Commun 2023;38:101492.

19. Mondal S, Roy C, Bhattacharyya S. Unravelling formation mechanism, thermal and oxidation stabilities of layered sub-micron MAB phase WAlB synthesized at open atmosphere. Mater Today Chem 2024;37:102004.

20. Zhang H, Ren G, Jia P, Zhao X, Ni N. Development of machine learning force field for thermal conductivity analysis in MoAlB: insights into anisotropic heat transfer mechanisms. Ceram Int 2024;50:13740−9.

21. Merz J, Cuskelly D, Richardson P. MAB phase-alumina composite formation via aluminothermic exchange reactions. Mater Lett 2024;360:135869.

22. Li X-H, Cui H-L, Yong Y-L, Zhang R-Z. Theoretical investigation of electronic, bonding and optical properties of nanolaminated boride WAlB. Mater Chem Phys 2018;212:122−30.

23. Liu Y, Jiang Z, Jiang X, Zhao J. New refractory MAB phases and their 2D derivatives: insight into the effects of valence electron concentration and chemical composition. RSC Adv 2020;10:25836−47.

24. Li H, Fan H, Su Y, Li Z, Chen S, Wei W, et al. Quaternary layered boride Ti_4MoSiB_2: a structure-function integrated high-temperature self-lubricating and negative-wear material. Adv Mater 2025;37:2418995.

25. Zhang D, Richardson P, Tu H, O'Connor J, Kisi E, Zhang H, et al. Radiation damage of MoAlB at elevated temperatures: investigating MAB phases as potential neutron shielding materials. J Eur Ceram Soc 2022;42:1311−21.

26. Guo Z, Han Z, Alkandari A, Khot K, Ruan X. First-principles prediction of thermal conductivity of bulk hexagonal boron nitride. Appl Phys Lett 2024;124:163906.

27. Zhou X-F, Zhou J. First-principles study on ultralow lattice thermal conductivity in $HfGeTe_4$. Mod Phys Lett B 2022;36: 2250123.

28. Luo X, Zhang T, Hu C-E, Cheng Y, Geng H-Y. First-principles studies on the structural, electronic and thermal transport characteristics of half-Heusler compounds LiXN (X=Mg, Zn). Solid State Commun 2023;366−367:115156.

29. Katre A, Togo A, Tanaka I, Madsen GKH. First principles study of thermal conductivity cross-over in nanostructured zinc-chalcogenides. J Appl Phys 2015;117:045102.

30. Yan S, Liu Z, Zhang J-H, Wei S, Zhang S, Chen X, et al. Raman spectrum and phonon thermal transport in van der Waals semiconductor $GaPS_4$. Appl Phys Lett 2024;125:022202.

31. Guo Z, Wang L, Wang K, Ren C, Guo R, Zhang Y, et al. Temperature dependent thermal conductivity of IIa diamond by laser excited Raman spectroscopy. Appl Phys Lett 2021;118:192104.

32. Devipriya CP, Deepa S, Udayaseelan J, Chandrasekaran R, Aravinthraj M, Sabari V. Quantum chemical and MD investigations on molecular structure, vibrational (FT-IR and FT-Raman), electronic, thermal, topological, molecular docking analysis of 1-carboxy-4-ethoxybenzene. Chem Phys Impact 2024;8: 100495.

33. Xu X, Goddard WA. The extended Perdew-Burke-Ernzerhof functional with improved accuracy for thermodynamic and electronic properties of molecular systems. J Chem Phys 2004;121:4068−82.

34. Perdew JP, Burke K, Ernzerhof M. Generalized gradient approximation made simple. Phys Rev Lett 1998;77:3865−8.

35. Kresse G, Furthmüller J. Efficient iterative schemes for ab initio total-energy calculations using a plane-wave basis set. Phys Rev B 1996;54:11169−86.

36. Li W, Carrete J, Katcho NA, Mingo N. ShengBTE: a solver of the Boltzmann transport equation for phonons. Comput Phys Commun 2014;185:1747−58.

37. Chen S-B, Guo S-D, Zeng Z-Y, Lv B, Xu M, Chen X-R, et al. Ultra-low lattice thermal conductivity induces high-performance thermoelectricity in Janus group-VIA binary monolayers: a comparative investigation. Vacuum 2023;213:112075.

38. Togo A. First-principles phonon calculations with phonopy and Phono3py. J Phys Soc Jpn 2023;92:012001.

39. Kroumova E, Aroyo MI, Perez-Mato JM, Kirov A, Capillas C, Ivantchev S, et al. Bilbao crystallographic server: useful databases and tools for phase-transition studies. Phase Transit 2003;76:155−70.

40. Hadi MA, Kelaidis N, Filippatos PP, Christopoulos S-RG, Chroneos A, Naqib SH, et al. Optical response, lithiation and charge transfer in Sn-based 211 MAX phases with electron localization function. J Mater Res Technol 2022;18:2470−9.

41. Li W, Lindsay L, Broido DA, Stewart DA, Mingo N. Thermal conductivity of bulk and nanowire $Mg_2Si_xSn_{1-x}$ alloys from first principles. Phys Rev B 2012;86:174307.

42. Xu L, Shi O, Liu C, Zhu D, Grasso S, Hu C. Synthesis, microstructure and properties of MoAlB ceramics. Ceram Int 2018;44: 13396−401.

43. Keshri SP, Pati SK. d-Orbital-Driven low lattice thermal conductivity in TiRhBi: a root for potential thermoelectric and microelectronic performance. ACS Appl Energy Mater 2022;5:13590−9.

44. Peng B, Zhang H, Shao H, Xu Y, Ni G, Zhang R, et al. Phonon transport properties of two-dimensional group-IV materials from *ab initio* calculations. Phys Rev B 2016;94:245420.

45. Ouyang T, Hu M. First-principles study on lattice thermal conductivity of thermoelectrics HgTe in different phases. J Appl Phys 2015;117:245101.

46. Palumbo M, Kisu K, Gulino V, Nervi C, Maschio L, Casassa S, et al. Ion conductivity in a magnesium borohydride ammonia borane solid-state electrolyte. J Phys Chem C 2022;126: 15118−27.

47. Smith KA, Ramkumar SP, Harms NC, Clune AJ, Cheong S-W, Liu Z, et al. Pressure-induced phase transition and phonon softening in h−Lu$_{0.6}$Sc$_{0.4}$FeO$_3$. Phys Rev B 2021;104:094109.

48. Lai H-E, Yoo RMS, Djire A, Balbuena PB. Investigation of the vibrational properties of 2D titanium nitride MXene using DFT. J Phys Chem C 2024;128:3327−42.

49. Skelton JM, Burton LA, Jackson AJ, Oba F, Parker SC, Walsh A. Lattice dynamics of the tin sulphides SnS$_2$, SnS and Sn$_2$S$_3$: vibrational spectra and thermal transport. Phys Chem Chem Phys 2017;19:12452−65.

50. Porezag D, Pederson MR. Infrared intensities and Raman-scattering activities within density-functional theory. Phys Rev B 1996;54:7830−6.